

Copyright  
by  
Sudharshanaraj Thiruppathiraj  
2021

**The Thesis Committee for Sudharshanaraj Thiruppathiraj  
Certifies that this is the approved version of the following thesis:**

**A Reactor Scale Gas Dynamics Model of an Industrial Multi-  
wafer Atomic Layer Deposition Reactor using Direct  
Simulation Monte Carlo Approach**

**APPROVED BY  
SUPERVISING COMMITTEE:**

Laxminarayan L. Raja, Supervisor

Gregory R. Zwernemann

Raghavendran Mahalingam

**A Reactor Scale Gas Dynamics Model of an Industrial Multi-  
wafer Atomic Layer Deposition Reactor using Direct  
Simulation Monte Carlo Approach**

**by**

**Sudharshanaraj Thirupathiraj**

**Thesis**

Presented to the Faculty of the Graduate School of

The University of Texas at Austin

in Partial Fulfillment

of the Requirements

for the Degree of

**Master of Science in Engineering**

**The University of Texas at Austin**

**May 2021**

Dedicated to my beloved family who have supported me in every aspect of  
my life.

*“Success is dependent on effort.”*

– **Sophocles**

## **Acknowledgements**

It is a great honor to have received my education at a very prestigious institution.

I must admit that the journey has been arduous, nevertheless a unique and exciting occasion every day. I am fortunate to have studied under an extraordinary committee whose passion is unfathomable. It is without any doubt that this journey was made possible by Dr. Laxminarayan Raja, my advisor and a mentor, whom I have always looked up to. He thoroughly understood my capabilities and patiently and admirably guided me with his clairvoyance even through the most challenging time. My dearest readers, Prof. Greg Zwernemann and Dr. Raghav Mahalingam were very supportive and enthusiastic in this endeavor. I thank them for their uncountable and invaluable advice as their student and the opportunity to assist in their lectures – through which my educational expenses were greatly met.

I had great pleasure of working with the very insightful Dr. Seung-Min Ryu of Samsung Electronics, who funded the project significantly. Irrefutably, his contribution to this project was crucial and is greatly appreciated.

Never would I have dreamt of a chance to revive my smoldering goal of pursuing a postgraduate degree until I had met Dr. Armand Chaput,

Dr. Philip Varghese, and Dr. Fabrizio Bisetti during my undergraduate years. To them, I shall remain grateful.

My friends and colleagues, in particular, Evrim Solmaz, David Meskill, Mark Maughmer II, Jeffrey Ramsey, and Scott Messec were a constant source of fun, encouragement, and assistance whenever I inclined most.

I would like to offer my sincerest gratitude to my well-wishers Dr. Satya Narimetla, Prof. Elizabeth Hutchins, and Dr. Samgopiraj Velraj at Tennessee Technological University.

I aspire to inspire the future generations more than I am, by my family, professors, and friends. Perhaps this might be the only possibility to repay an insignificant portion of all the favor I have received from those I will revere forever.

# **Abstract**

## **A Reactor Scale Gas Dynamics Model of an Industrial Multi-wafer Atomic Layer Deposition Reactor using Direct Simulation Monte Carlo Approach**

Sudharshanaraj Thiruppathiraj, MSE  
The University of Texas at Austin, 2021

Supervisor: Laxminarayan L. Raja

Atomic layer deposition (ALD) using multi-wafer batch reactors has now emerged as the manufacturing process of choice for modern microelectronics at a massive scale. Stringent process requirements of thin film deposition uniformity within wafer (WiW) and wafer-wafer (WTW) in the batch, film conformity along submicron wafer features, thin film quality, and the utilization of expensive precursors in the reactor dictate ALD reactor design and process parameter optimization. This research discusses a particle-based direct-simulation Monte Carlo (DSMC) of the full reactor scale simulation that overcomes the low Knudsen number limitation of typical

continuum computational fluid dynamics (CFD) approaches used for modeling low-pressure ALD reactors. A representative industrial multi-wafer batch reactor used for the deposition of Si-based thin films with  $N_2$  and  $Si_2Cl_6$  (hexachlorodisilane - HCD) as process feed gases with pressures in the range 43 Pa to 130 Pa and uniform reactor temperature of 600°C is simulated. The model provides detailed insights into the flow physics associated with the transport of the precursor species from the inlets, through wafer feed nozzles, into the inter-wafer regions, and finally through the outlet. The reactor operating conditions are shown to be in the slip/transitional flow regime for much of the reactor volume and especially the feed gas nozzle and inter wafer regions (where the Knudsen number approaches  $\sim 0.2$ ), justifying the need for a high-Knudsen number DSMC approach as in this work. For the simulated conditions, the non-uniformity of precursor species immediately above the wafer surface is predicted to be within  $< 1\%$  for a given wafer and  $< 2\%$  across the entire multi-wafer stack. Results indicate that higher pressure degrades WiW and WTW uniformity. A precursor-wafer interaction efficiency of  $\sim 99\%$  is observed, irrespective of chamber pressure.

## Table of Contents

List of Figures .....	x
Chapter 1 Introduction .....	1
1.1 Limitations of Chemical Vapor Deposition.....	1
1.2 Industrial Multi-wafer Batch Reactors .....	2
1.3 Motivation.....	4
Chapter 2 Model Description.....	7
2.1 The Design of Thermal ALD Batch Reactor .....	8
2.2 The Direct-Simulation Monte Carlo Approach .....	10
2.3 Computational Mesh.....	14
2.4 Operating Conditions.....	16
Chapter 3 Results and Discussion.....	20
3.1 Flow Characteristics .....	21
3.2 Precursor Concentration Profile.....	30
3.3 Precursor-Wafer Interaction Efficiency.....	38
Chapter 4 Summary .....	40
4.1 Future Work.....	42
References.....	43
Vita.....	48

## List of Figures

Figure 2.1: A cutaway of the multi-wafer batch ALD reactor showing main features of relevance to this study. The path of the gas is highlighted for the central inlet. ....	8
Figure 2.2: The upper section of the computational domain showing mesh features.....	16
Figure 3.1: Cross section of the reactor showing pressure profiles for the intermediate case. [The range of the contours are chosen to highlight only the pressure variations within the reactor volume and not the inlet nozzles.].....	21
Figure 3.2: Azimuthally averaged pressure (Pa) at various radial locations on 25 wafers for all three cases. [In the figure, ‘dot’ markers correspond to 43 Pa, ‘triangles’ to 86 Pa, and ‘circles’ to 130 Pa. This notation is used for all figures below.] .....	23
Figure 3.3: (a) Velocity streamlines as seen from the side, (b) from the top of the reactor – outlet is on the top, and (c) velocity contours along the reactor symmetry plane for intermediate pressure 86 Pa case.....	25

Figure 3.4: Cross section of the reactor center showing (a) pressure, (b) temperature, and (c) velocity streamlines of inlet jets for the intermediate pressure (83 Pa). .....27

Figure 3.5: Cross section of the reactor showing number density profiles of HCD for the intermediate 86 Pa case. (The range of the contours are chosen to highlight only the pressure variations within the reactor volume and not the inlet nozzles.) .....30

Figure 3.6: Cross sections of (a) #4, (b) #13, and (c) #22 wafers showing number density profiles of HCD for lowest pressure (43Pa). [Note the simulation results are mirrored about the half plane for clarity].....32

Figure 3.7: Cross sections of (a) #4, (b) #13, and (c) #22 wafers showing number density profiles of HCD for intermediate pressure (86 Pa). [Note the simulation results are mirrored about the half plane for clarity].....33

Figure 3.8: Cross sections of (a) #4, (b) #13, and (c) #22 wafers showing number density profiles of HCD for highest pressure (130Pa). [Note the simulation results are mirrored about the half plane for clarity].....	34
Figure 3.9: Azimuthally averaged incident surface flux of HCD ( $\#/m^2\cdot s$ ) sampled at various locations on the wafers for all three pressure cases. ....	36

# Chapter 1

## Introduction

Scaling trends in the semiconductor manufacturing industry have traditionally been dictated by the Moore's Law, which states that the number of transistors on an integrated circuit roughly increases twice every two years. The primary approach to achieving this trend is to shrink feature sizes on chips [1]. This need for miniaturization of microelectronics has driven semiconductor companies to extend it in three dimensions and fabricate at 5 nm scales and lower.

### 1.1 Limitations of Chemical Vapor Deposition

With increasing demand for good performance and capacity, the latest flash memory devices are based on 3D vertical-NAND (V-NAND) architectures. The challenge with 3D V-NAND memory lies in the fabrication of very high aspect ratio channel holes requiring etching and deposition of very thin and conformal layers of nitrides or oxides of silicon with atomic layer precision. Classical techniques like chemical vapor deposition (CVD) have been used to construct the nano-scale features,

although they require the operation at undesirably high temperature, in temperatures excess of 700 °C [2] and poor step coverage. The atomic layer deposition (ALD) technique is an alternative to CVD and can achieve atomic precision in the deposition process [2] [3] [4] [5]. This precision is achieved through the deposition of individual atomic layers on the surface through separate self-limiting reaction steps that are repeated in cycles [6]. Each step in an ALD cycle involves the introduction of a specific source precursor and reactant gases to build an atomic layer partially, followed by one or more steps that involve a different gas exposure to complete a single atomic layer [5]. The process is inherently slow and extremely time-consuming to complete a single ALD film stack versus a similar CVD process.

## **1.2 Industrial Multi-wafer Batch Reactors**

Although precision manufacturing requirements have forced single-wafer processing as a necessity in several semiconductor manufacturing unit steps [7], batch processing of many wafers at the same time is desirable to increase throughput and minimize costs [8]. Fortunately, batch processing for ALD has proven a success in large throughput semiconductor manufacturing,

although many issues with this processing approach remain unique and require extensive study for a specific thin film deposition system.

Industrial batch processing reactors involves placing a vertical or horizontal stack of several tens of wafers at the same time [9] [10]. However, the vertical type of batch process has been mostly used in the industry due to better uniformity of wafers and less footprint for the equipment. Batch reactors typically operate in a hot wall configuration, with the entire system being maintained at a single operating temperature, which in itself poses a complicated thermal design and control problem. A series of injectors carry source precursor, reactant, and carrier gases into the reactor that diffuse into the inter-wafer spaces and interact with the wafer surface where the ALD reactions occurs. The remaining precursor gas is typically removed from the reactor by a common exhaust.

The uniformity of ALD processes must be ensured across the wafer area for each wafer, and the same deposition conditions and uniformity must be ensured for all wafer across the batch reactor wafer stack. This can be achieved by the positioning of individual gas injectors for each wafer in the stack and the gradual rotation of the entire wafer stack [10]. However, in practice, despite the individual wafer-level organization of the precursor flow, a large pressure differential across the length of the reactor volume means that

uniformity across the wafer stack can be compromised. For example, the gas flow rates can vary gradually between different inter-wafer gap regions, and consequently, the deposition rate can be different on different wafer surfaces for the same process batch. Despite the wafer rotation, single wafer uniformity can also be difficult because the flow from each injector nozzle can exit with high momentum and spread non-uniformly over the wafer surface. Overall, within-wafer (WiW) and wafer-wafer (WTW) uniformity, step-coverage, deposition time, and precursor consumption are still the main concerns of the ALD batch process.

### **1.3 Motivation**

While the deposition chemistry of various ALD processes has been studied widely through reaction engineering and *ab initio* modeling approaches [11] [12], the reactor design, and its optimization is traditionally done through cut-and-try approaches by experienced equipment engineers and increasingly through the use of computational fluid dynamics (CFD) tools to address specific flow components in the reactor, if not the reactor as a whole [13] [14] [15] [16]. A few studies, in literature, have reported full reactor modeling of batch ALD systems, albeit with some simplifications compared

to actual industrial process reactors [2] [17] [18] [19]. These studies have provided insights into several of the questions mentioned, e.g., cross-wafer and inter-wafer uniformity as a function of the reactor operating conditions.

Despite the usefulness of CFD modeling, a key question on the validity of continuum fluid modeling in low-pressure ALD reactor remains. At low pressures, the mean free path of gas molecules ( $\lambda$ ) can be comparable to critical dimensions of flow facing parts of the reactor ( $l_c$ ). As an example, for the conditions of interest in the study reported in this thesis, i.e., a pressure range of 43 Pa to 130 Pa and temperature of 600 °C, the mean free path ranges from 0.3 mm to 3 mm in the wafer zone depending on the species concentration and pressure, which is comparable to the gas distribution nozzle diameter of 2 mm, and the 19.2 mm inter-wafer gap. In other words, the local Knudsen number  $Kn = \frac{\lambda}{l_c}$  around the inter-wafer gap is estimated to be  $\sim 0.2$  i.e., in the slip-transition region [20], invalidating the accuracy of the CFD models that require  $Kn \ll 1$  [21]. Particle-based models for gas transport in these systems is more appropriate and can preserve the fidelity of the model in all regions of a batch reactor.

A purely gas kinetic model for a full scale ALD reactor is the subject of this research. A Direct-Simulation Monte Carlo (DSMC) approach for

modeling a representative industrial thermal ALD batch reactor is considered here. The gas dynamics of flow through the reactor, mixing of the precursor molecules with the inert carrier gas stream in the inter-wafer gap region, uniformity of process across a wafer, and across different wafers in the stack are described. Insights into the non-continuum effects are provided to assess the need for DSMC modeling of such reactor systems. The DSMC model is described in Chapter 2, simulation results and discussions are presented in Chapter 3, and the conclusion in Chapter 4.

## Chapter 2

### Model Description

A single step of a multi-step ALD process is considered for the deposition of  $\text{Si}_x\text{N}_y$  film using  $\text{Si}_2\text{Cl}_6$  (hexachlorodisilane or HCD) as the precursor [22]. The precursor is transported into the reactor through the nozzle using  $\text{N}_2$  as the carrier gas. Previous studies [11] [23] have shown that the HCD precursor is stable in the gas phase at the temperatures of interest in this study, and hence gas phase reactions are neglected. Furthermore, the ratio of molecules that adsorb to that impinge upon a surface in the same period, i.e., sticking coefficient for the precursor at the active surface is low ( $\sim 10^{-5}$ ) at the ALD process temperatures of interest. Hence, the surface appears mostly non-reactive to the HCD molecules [11] and it takes several minutes to complete the source supply step for deposition of hole patterns with aspect ratio of 100 or more in the batch process. This longer processing time in the batch reactor has a major influence on uniformity than in single wafer process.

## 2.1 The Design of Thermal ALD Batch Reactor

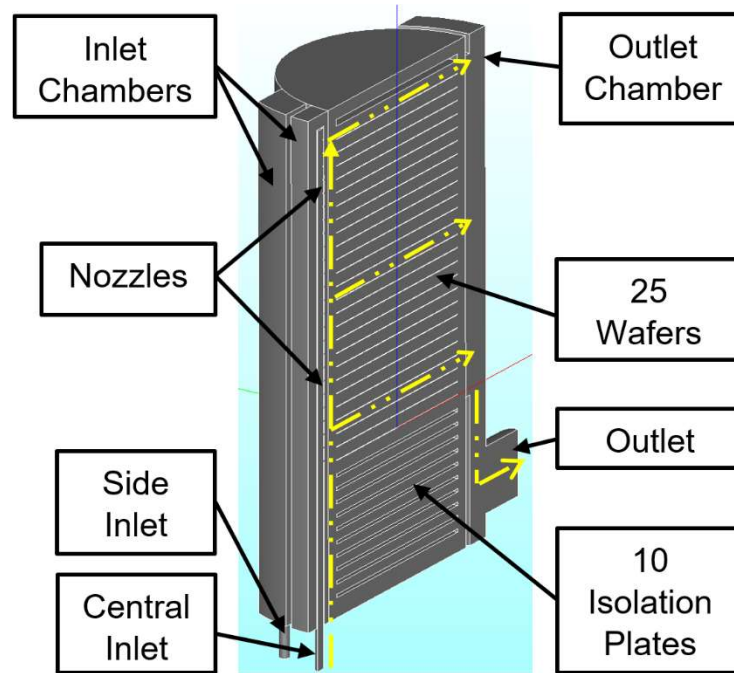


Figure 2.1: A cutaway of the multi-wafer batch ALD reactor showing main features of relevance to this study. The path of the gas is highlighted for the central inlet.

The chamber design used in this study is based on a representative industrial full-scale reactor with a vertically stacked multi-wafer and crossflow system of diffusion flow laterally across the wafer patented by Yoshida et al. [10]. Figure 2.1 shows a schematic of the reactor geometry with a half-symmetry cut through the center of the reactor. The external

dimensions of the reactor are roughly 0.5 m × 0.35 m × 0.75 m (L×W×H). This batch reactor houses a 25-wafer stack with a pitch of 20mm, and each silicon wafer has a diameter of 300 mm and a thickness of 0.8 mm. The wafers are unpatterned. The wafers are uniformly spaced from each other at an inter-wafer gap of 19.2 mm. An annular gap of 10 mm exists between the edge of the wafers and the inner radial wall of the reactor tube. To operate the reactor at high temperature, this gap is necessary to maintain a sufficient tolerance for differential thermal expansion of the different components in the reactor and to accommodate the rotational tolerance of the wafer stacked boat. This gap is, however, detrimental to obtain uniform thickness of the deposited films and to effectively transport the precursor to the wafers since it provides an alternative flow path for the process gases that can completely bypass the wafer region. This undesirable flow path is termed as “bypass flow”, in the study.

There are three inlet gas feed nozzles with gas injection holes in each separate chamber space from which the inlet gases can be injected into the central chamber containing the wafer stack. Feeding of gases is done through the two outer nozzles (*Side Inlet*) supplying carrier N<sub>2</sub> gas while the central nozzle (*Central Inlet*) supplying a mixture of N<sub>2</sub> carrier gas and HCD precursor. The gases entering from the inlets are directly transported into

each of the 25 inter-wafer gaps through 25 nozzle holes with a diameter of 2 mm in each nozzle. The gas flow direction in the inlet manifold is from bottom to top and the top of each nozzle is capped, thus ensuring all the inlet flow in each nozzle exits only through the 25 holes. On entering the reactor volume, feed gas diffuses between the inter-wafer space, reacts with the wafer surface, and flows out to a cylindrical outlet port located at the bottom side of the reactor.

## 2.2 The Direct-Simulation Monte Carlo Approach

A multi-species DSMC approach implemented in *VizGrain* software package [24] [25] [32] is used to model gas transport, inter-species gas phase mixing, and the interaction of the precursor molecules with the reactor components and the wafer surface. The DSMC model is a particle-based full kinetic representation for the gas flow [21]. Representative particles are used to simulate the motion of individual real particles in the gas. The representative particles are also called “simulated particles”, and each simulated particle has a mass  $m_p$  that is the same as a real particle (atom or molecule) it represents. In order to make a simulation tractable, each simulated particle is assigned a statistical weight  $\mathcal{F}$ , where  $\mathcal{F}$  is the number of

real particles that a single simulated particle represents.  $\mathcal{F}$  needs to be large. For example, in the simulation, it is  $\sim 10^{13}$ . This value is chosen to give about 5 particles per cell for transition and slip flow regimes at which the reactor operates [27]. The motion of a particle is governed by Newton's laws. Mathematically, it is represented as:

$$m_p \frac{d\vec{c}_p}{dt} = \vec{F}_p \quad (1)$$

$$\frac{d\vec{x}_p}{dt} = \vec{c}_p \quad (2)$$

where,  $\vec{x}_p$  is the particle position,  $\vec{c}_p$  is the particle velocity, and  $\vec{F}_p$  is the force acting on the particle. Equations (1) and (2) are time-integrated using a leap-frog finite-difference time integration approach with a time step  $\Delta t$ . In the absence of forces acting on the particle (e.g., in the case of a neutral gas), the particles execute straight-line trajectories until they are interrupted by very brief collision events with other particles or with solid boundaries. Collisions among particles are treated using a unique collision sampling technique called the DSMC (in fact, the classification DSMC refers specifically to the collision algorithm in a particle method but is used generally to describe the particle-based modeling approach as a whole).

The DSMC model executes a gas collision among particles in close vicinity of each other. At any given time, all particles within a small cell volume in the domain are assumed candidates for executing collisions. The collisions are solved by determining the probability of collision ( $P_{coll}$ ) between any two particles within a cell of volume  $V_{cell}$  and is determined as:

$$P_{coll} = \mathcal{F} \frac{\sigma_r g_r}{V_{cell}} \Delta t \quad (3)$$

Here,  $g_r$  is the relative speed between the two particles and  $\sigma_r$  is the collision cross section for the collision pair. In general, the approach is to pick all possible collision pairs within a cell, i.e.  $\frac{1}{2} N_a N_b$  where  $N_a$  and  $N_b$  are the number of simulated particles of species  $a$  and  $b$ , respectively (for example,  $N_2$  and HCD are the two species in this problem), and execute the collision if a uniform random number  $\mathcal{R}_{rand} = (0,1]$  is such that  $\mathcal{R}_{rand} < P_{coll}$ . This is then repeated for all cell volumes in the domain before the next particle move step in equations (2) and (3) are repeated. The above approach is, however, computationally costly, and a variation of the Null-Time-Counter (NTC) method is used in this study. Here the maximum expected value of the product of  $\sigma_r$  and  $g_r$  is estimated, i.e.  $(\sigma_r g_r)_{max}$ , and the maximum collision probability,

$$P_{coll,max} = \mathcal{F} \frac{(\sigma_r g_r)_{max}}{V_{cell}} \Delta t \quad (4)$$

is evaluated for each cell. Instead of selecting all possible collision pairs in a cell, a smaller fraction of the pairs  $N_{coll,pair}$  is selected for collision as,

$$N_{coll,pair} = \frac{1}{2} N_a N_b P_{coll,max} \quad (5)$$

These pairs then collide if a uniform random number  $\mathcal{R}_{rand} < \frac{P_{coll}}{P_{coll,max}}$

. The value of  $(\sigma_r g_r)_{max}$  for each cell is updated during the simulation so a best estimate is available at all times for calculating  $P_{coll,max}$ . Overall, the computational saving with the NTC approach can be considerable for large-scale problems with a large number of simulated particles.

The above DSMC approach requires the entire computational domain to be divided into non-overlapping, continuous cell volumes, which is achieved using a standard, unstructured mesh, as in the case of CFD simulations. The same mesh is also useful in calculating average fluid properties by calculating the ensemble average properties of the simulated particles with each cell volume in the domain. In the case of the DSMC method, the mesh resolution requirement and particle count requirement (adjustable by the statistical weight  $\mathcal{F}$ ) is such that a few 10s to 100s of

particles must reside within each cell for sufficient collision and average fluid property statistics. The time step  $\Delta t$  is chosen such that the particles only transit a fraction of a cell at each time step.

Boundary conditions include the inlets, walls, and outlets. At the inlets, all particles are assumed to enter with a specified Maxwellian inflow flux for the individual species at a specified inflow temperature. Particles from the interior that impinge at the inlet are assumed to be reflected back diffusely at the specified inlet temperature, which effectively forces the correct gas inflow into the reactor. All particles interacting with the reactor walls are assumed to thermally accommodate at the wall and then reflect off diffusely from the surface dictated by a Maxwellian distribution at the surface temperature. At the outlet, a particle reflection fraction parameter ( $f_{\text{out}}$ ) of the particles that impinge on the outlet surface are assumed to reflect back diffusely. As discussed below, in the simulations this fraction is defined by repeated trials to achieve an overall specified pressure in the reactor.

### **2.3 Computational Mesh**

Due to a vertical symmetry in the geometry about the midplane of the reactor, the simulations consider only half of the actual reactor domain with a

plane of symmetry boundary separating the two halves. The mesh for the DSMC model is generated using Salome, an open-source geometry creation, and meshing tool [26].

An unstructured mesh comprising 1.21 million tetrahedral cells was constructed. Section of the mesh is shown in Figure 2.2. Resolution requirements in the mesh were dictated by the need to resolve flow-relevant geometric features of the reactor as well as requirements imposed by the DSMC algorithm discussed above. At the highest pressure considered in this study, mean free paths of  $N_2$  and HCD mixture was estimated to be between 0.3 mm to 3 mm. Cell sizes were chosen based on mean free paths of  $N_2$  and HCD, the ability to maintain geometric fidelity, and the necessity to achieve a significant number of particles in each cell for better numerical results [27]. Cell diameters on the wafers are about 8 mm, and in the inter-wafer gap, they are around 5 mm, as shown in Figure 2.2.

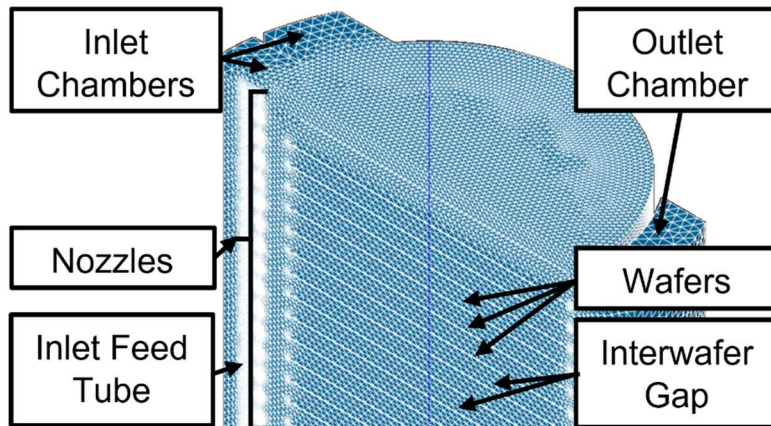


Figure 2.2: The upper section of the computational domain showing mesh features.

## 2.4 Operating Conditions

The reactor is assumed to operate at chamber pressures of 43 Pa, 86 Pa, and 130 Pa and a uniform wall temperature of 600 °C (873 K). Although a practical reactor will experience temperature non-uniformities, the consideration of thermal state of the reactor is outside the scope of this study. Here the focus is only on the rarefied flow physics in the ALD reactor. The *Central Inlet* provides a mixture of HCD precursor gas along with carrier N<sub>2</sub> gas in the volume ratio 1:5 totaling 1.2 SLPM (standard liter per minute), 2.4 SLPM, and 3.6 SLPM for the three operating pressures 43 Pa, 86 Pa, and 130

Pa, respectively. Similarly, the outer feed nozzles – the two *Side Inlets* (note only one side inlet is included in the simulations owing to the symmetry considerations) provide pure N<sub>2</sub> gas at 0.5 slm, 1.0 slm, and 1.5 slm, respectively, for the three pressure cases. The inlets, wall, and outlet temperatures are all taken to be 600 °C.

A time step  $\Delta t$  of 0.1 ms was chosen based on the molecular speed at the operating conditions and cell sizes in the wafer region. Gas phase reactions, mainly decomposition of HCD, is insignificant for the reactor conditions described above [5] [28] [29]. Hence to ease computational overhead, a non-reactive chemistry of single precursor (HCD) transported by a carrier gas (N<sub>2</sub>) is used to describe the gas feed process in the reactor. A statistical weight of  $\mathcal{F} = 1 \times 10^{13}$  for a chamber pressure of 43 Pa,  $\mathcal{F} = 2 \times 10^{13}$  for intermediate pressure of 86 Pa, and  $\mathcal{F} = 3 \times 10^{13}$  for the highest pressure of 130 Pa is used, which corresponds roughly to 15 million particles simulated for each reactor condition. These statistical weight choices ensure about five particles per cell for transitional flows [27].

The DSMC collision algorithm requires specification of molecular mass and collision cross sections for the three possible binary collision pairs in the two species gas mixture. These properties for N<sub>2</sub> are taken to be

$4.7 \times 10^{-26}$  kg and  $4.3 \times 10^{-19}$  m<sup>2</sup> [30], and for HCD to be  $4.4 \times 10^{-25}$  kg and an estimated cross-section of  $4.4 \times 10^{-18}$  m<sup>2</sup>, about 10 times that of N<sub>2</sub>. The corresponding collision cross sections  $\sigma_r$  are calculated assuming a hard sphere molecular model for each collision pair [10].

Pressure control in the reactor requires careful attention. In practice, the pressure in the reactor is set by the total feed gas flow rate into the reactor and the outflow impedance at the pump as characterized by the effective blockage of the pumping system to the outflowing gas molecules [31]. A calibration study is first performed, where a fraction of the molecules in that impinge on the outflow boundary  $f_{\text{out}}$  are reflected back into the domain.  $f_{\text{out}}$  effectively mimics flow impedance of the pump.  $f_{\text{out}}$  is calibrated in the study by running the DSMC simulations over a range of  $f_{\text{out}}$  values for fixed feed gas inflow rates, thus giving a correlation between the reactor pressure and the value of  $f_{\text{out}}$ . A value of  $f_{\text{out}} = 0.11$  is determined based on a calibration of the conditions from the case with lowest operating pressure of 43 Pa. This value of  $f_{\text{out}}$  is assumed fixed for all simulations.

The initial state of the reactor is assumed to correspond to vacuum and the simulations start with a flow of particles through the inlets. All simulations were performed on the Stampede 2 supercomputer at the Texas

Advanced Computing Center (TACC) at the University of Texas at Austin.  
Each simulation run typically used 480 cores divided across 10 nodes. The  
CPU time for the simulations was typically 48 hours.

## **Chapter 3**

### **Results and Discussion**

The flow residence times for reactors depend on geometry of the components, pressure, temperature, gas composition, and mass flow rate. Using the approach by Lankhorst et al. (refer Eq.11 in [17]), the flow residence times is estimated to be about 0.45 s for all three cases. The simulations ran to about 8.5 s of physical time, i.e., about twenty times the estimated residence time to ensure a steady state. The total number of simulated particles in the domain also remained nearly constant during this period confirming a steady state. The results presented below are time-averaged over relatively long periodic intervals of 0.75 s to reduce statistical noise in the averaged gas properties. While a longer time averaging will yield results with further improvements to the statistical noise, the chosen value was purely due to single run time restrictions on the supercomputing nodes at TACC.

### 3.1 Flow Characteristics

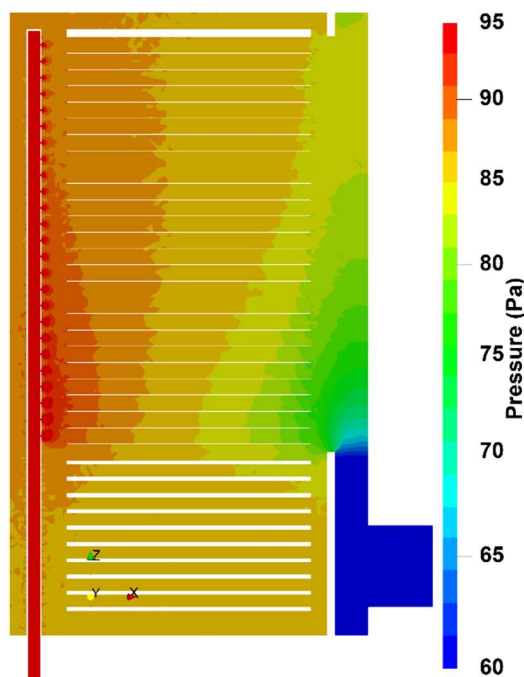


Figure 3.1: Cross section of the reactor showing pressure profiles for the intermediate case. [The range of the contours are chosen to highlight only the pressure variations within the reactor volume and not the inlet nozzles.]

The steady state result for the pressure contours across the symmetry plane cross section of the reactor at 86 Pa is shown in Figure 3.1. The pressure is significantly higher in the feed gas inlet nozzles  $\sim 10^4$  Pa than the pressure in the reactor volume owing to flow constriction at the small 2 mm dia. nozzles that feed each inter-wafer gap independently. (Note that in Figure 3.1,

maximum pressure contour is taken as 95 Pa corresponding to the highest pressure within the reactor volume. The pressure in the inlet nozzles is therefore shown as saturated at this value.) The pressure, however, drops rapidly along the length of the inlet tube as it flows from the bottom to the top and loses mass as the gas effuses out through each nozzle. Once the gas exits the nozzles to enter the reactor volume the pressure drops along the flow direction and varies over a range from about 95 Pa to 70 Pa, as it flows through wafers, along the bypass regions, and finally out through the outflow. Although the operating pressure is characterized by a single average value (86 Pa) in this case, actual pressure within the wafer zone varies by almost 15%.

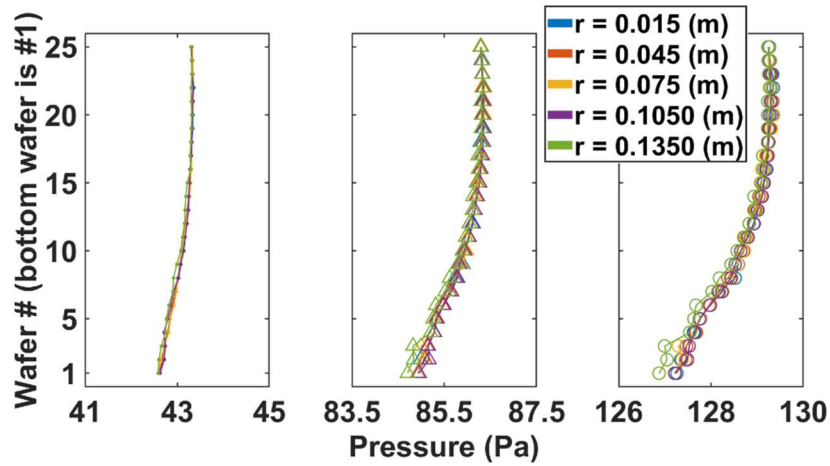


Figure 3.2: Azimuthally averaged pressure (Pa) at various radial locations on 25 wafers for all three cases. [In the figure, ‘dot’ markers correspond to 43 Pa, ‘triangles’ to 86 Pa, and ‘circles’ to 130 Pa. This notation is used for all figures below.]

Figure 3.2 shows the azimuthally averaged pressure profiles at fixed radial locations for all 25 wafers in the stack. The azimuthal averaging is motivated by the wafer rotation that provides an averaged flow environment across the wafer. The variation of the averaged pressure on each of the 25 wafer surfaces is found to be negligible at different radial locations, with the highest radial variations of about 0.4% observed only for the highest pressure (130 Pa case) and at the bottom-most wafers in the stack. The azimuthally averaged wafer pressure increases slightly from the bottom-most wafer #1 to the top-most wafer #25 with the highest variation of about 2% observed for

the bottom-most wafer in the 130 Pa case. It must be noted that the pressure upstream of each nozzle decreases from the bottom-most nozzle to the top-most nozzle, but the average pressure variation on the wafers is opposite due to the influence of the low pressures at the outflow end of the wafer stack and the azimuthal averaging.

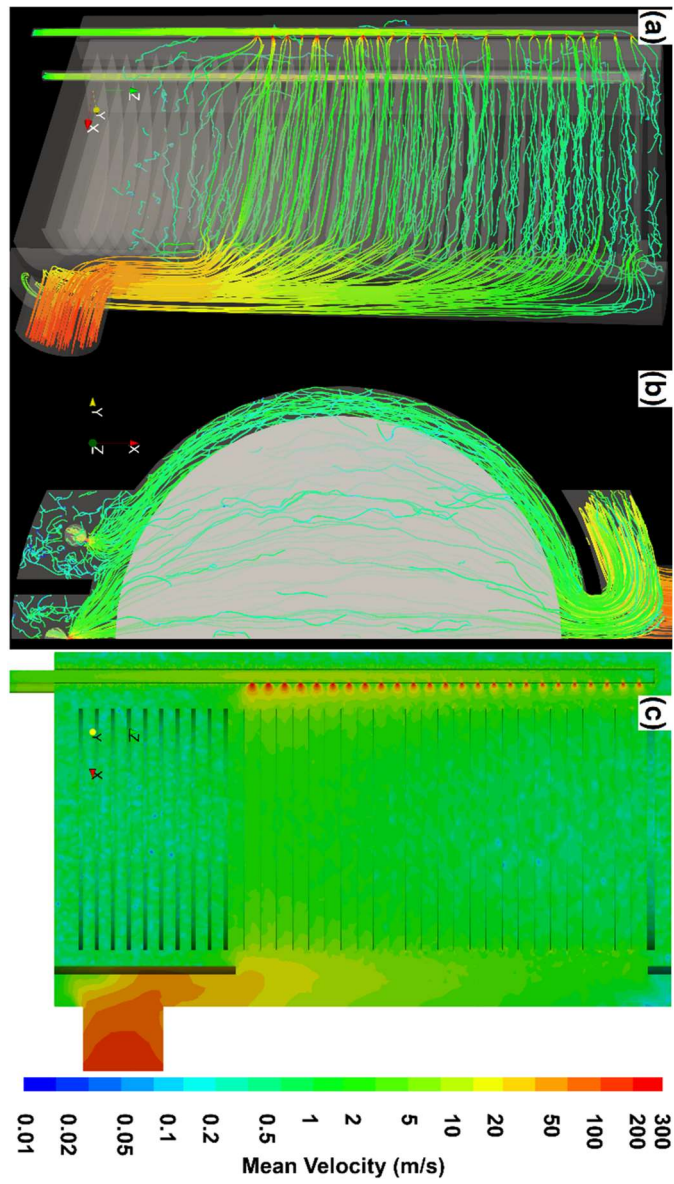


Figure 3.3: (a) Velocity streamlines as seen from the side, (b) from the top of the reactor – outlet is on the top, and (c) velocity contours along the reactor symmetry plane for intermediate pressure 86 Pa case. (Rotated 90° clockwise.)

Figure 3.3 shows the flow velocity streamlines from the side of the reactor and panel (c) from the top of the reactor for the 86 Pa case. The streamlines are colored according to flow speed shown on the legend to the right in the Figure 3.3. The streamlines indicate the flow exits the individual nozzles and rapidly expands within the reactor volume. The side view (panels (a) and (c) in Figure 3.3) shows the flow from the nozzle (the central inlet nozzles are more clearly seen in panel (b) enters the inter-wafer gap and exits the opposite end of the wafer stack into the outlet region of the reactor volume. The top-down view (panel (b) in Figure 3.3) indicates a significant fraction of the streamlines, especially from the side inlet nozzle, bypass the inter-wafer region altogether. The flow from the central inlet nozzles is more confined and enter the inter-wafer gap without as much bypass loss as the side inlet nozzle flows. The panel (c) on Figure 3.3 shows the flow velocity contours on the symmetry plane of the reactor. The peak flow velocity of about 300 m/s occurs at the individual nozzle exit locations and slow down significantly as they flow through the reactor volume before being accelerated again as it exits the reactor in the outlet pump port region.

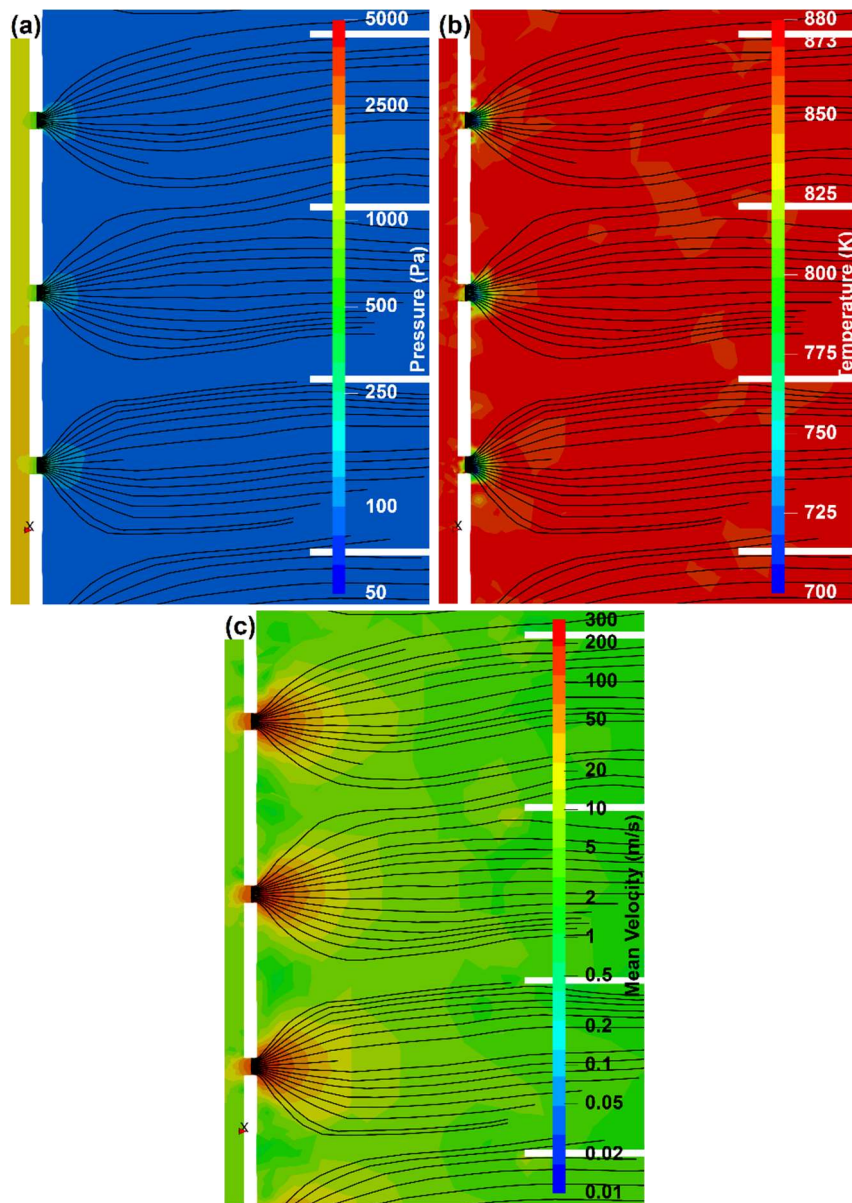


Figure 3.4: Cross section of the reactor center showing (a) pressure, (b) temperature, and (c) velocity streamlines of inlet jets for the intermediate pressure (83 Pa).

A closeup view of the flow variables in the nozzle region around the wafer #12 through #15, near the mid-section of the reactor, is shown in Figure 3.4. The inlet nozzle is on the left of each panel and the reactor volume is to the right of the nozzle wall and nozzle exits. The edges of the wafers are seen to the right of each panel. As mentioned earlier, the inlet nozzle pressure is significantly higher than the reactor volume and is about 1500 Pa for the central nozzle shown and drops rapidly as it flows through the nozzle and enters the reactor where the pressure is around 90 Pa. The pressure between the nozzle and the reactor is almost entirely dropped within the nozzle. The temperature is uniform at 873 K (600°C) in the nozzle and drops rapidly to a minimum temperature of about 700 K as it accelerates through the nozzle. The temperature quickly recovers to that of the reactor volume temperature of 873 K. The flow velocity is seen to accelerate to a peak value of about 310 m/s as it is constricted through the nozzle region and slows down to much lower values of  $\sim 1$  m/s within the reactor volume.

Despite the rapid acceleration of the flow through the nozzle the flow remains subsonic throughout with peak Mach numbers not exceeding about 0.6. This is due to speed of sound being around 530 m/s at 700 K and the maximum flow velocity is 310 m/s giving a locally subsonic flow throughout. The residence time of the flow in the nozzle region  $\tau_{\text{nozzle}}$  can be estimated

by the ratio of a characteristic length scale  $d_{nozzle}$  ( $\sim 2$  mm) given by the nozzle diameter to the peak flow velocity  $u_{peak}$  ( $\sim 300$  m/s) and is calculated around 7 microseconds. The kinematic viscosity of the flow  $\nu_{visc}$  is also estimated by the Sutherland's formula for nitrogen at 600 °C is about  $98 \times 10^{-6}$  m<sup>2</sup>/s. Therefore, the viscous diffusion length scale estimated as  $l_{visc} = \sqrt{\nu_{visc} \tau_{nozzle}} \sim 7 \times 10^{-10}$  m. Since  $l_{visc} \ll d_{nozzle}$  the flow in the individual nozzle region can be considered inviscid and adiabatic, explaining the rapid drop in temperature to about 700 K as the flow navigates through the nozzle. The flow in the nozzle region can therefore be summarized as a high subsonic inviscid flow.

A similar estimate of the residence time in the inter-wafer region  $\tau_{wafer}$  using an average flow velocity  $u_{wafer}$  of about 1 m/s and a characteristic length scale of the wafer diameter  $d_{wafer} = 0.3$  m, gives a  $\tau_{wafer} \sim 0.3$  s. Here the Mach number approaches zero. The corresponding viscous diffusion length scale in the inter-wafer region  $l_{wafer} = \sqrt{\nu_{visc} \tau_{wafer}} \sim 5$  mm. This length is comparable to the inter-wafer gap of 19.2 mm. Hence, the flow in the inter-wafer region can be summarized as a highly viscous dominated Stokes' flow.

## 3.2 Precursor Concentration Profile

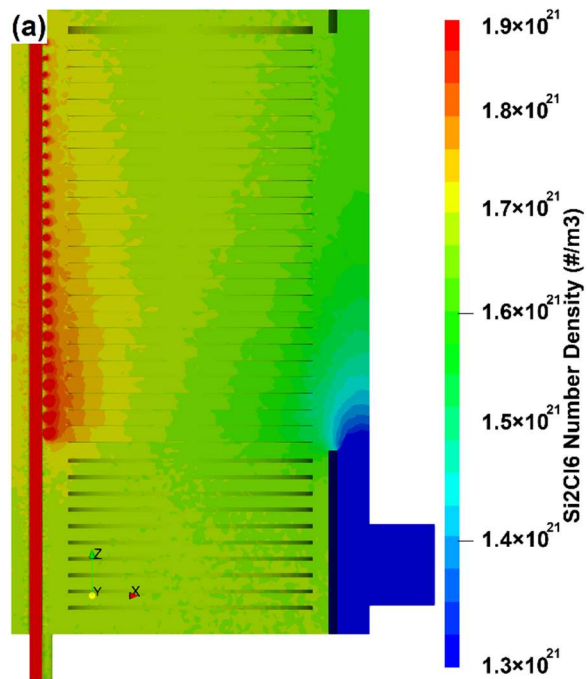


Figure 3.5: Cross section of the reactor showing number density profiles of HCD for the intermediate 86 Pa case. (The range of the contours are chosen to highlight only the pressure variations within the reactor volume and not the inlet nozzles.)

Figure 3.5 shows the number density contours of the active precursor HCD on the symmetry plane of the reactor for the intermediate pressure 86 Pa case. The precursor flows into the reactor only through the central inlet nozzles along with the N<sub>2</sub> carrier gas and then mixes with the pure N<sub>2</sub> gas

streams from the side nozzles. The HCD density is highest at the bottom-most nozzle that is adjacent to the wafer #1 and gradually decreases in the upper regions of the wafer zone. In a reactive environment, the HCD density changes in the reactor are a consequence of three factors: changes in total gas density resulting from pressure and temperature changes, dilution of the HCD molecules due to mixing with the side inlet pure N<sub>2</sub> gas streams, and decomposition to reaction products owing to gas and surface reactions. For the reactor conditions in this study, the temperature is mostly uniform at 873 K, no homogeneous reactions occur in the gas phase, and the surface consumption of HCD is assumed zero due to the negligibly low sticking probability (estimated at  $\sim 10^{-5}$  in [11]). As a result, the HCD density changes are due only to pressure variation in the reactor and mixing of HCD with the carrier gas side inlet streams. Hence, the HCD density changes seen in Figure 3.5 on the symmetry plane can be directly related to the pressure changes seen in Figure 3.1 on the same plane.

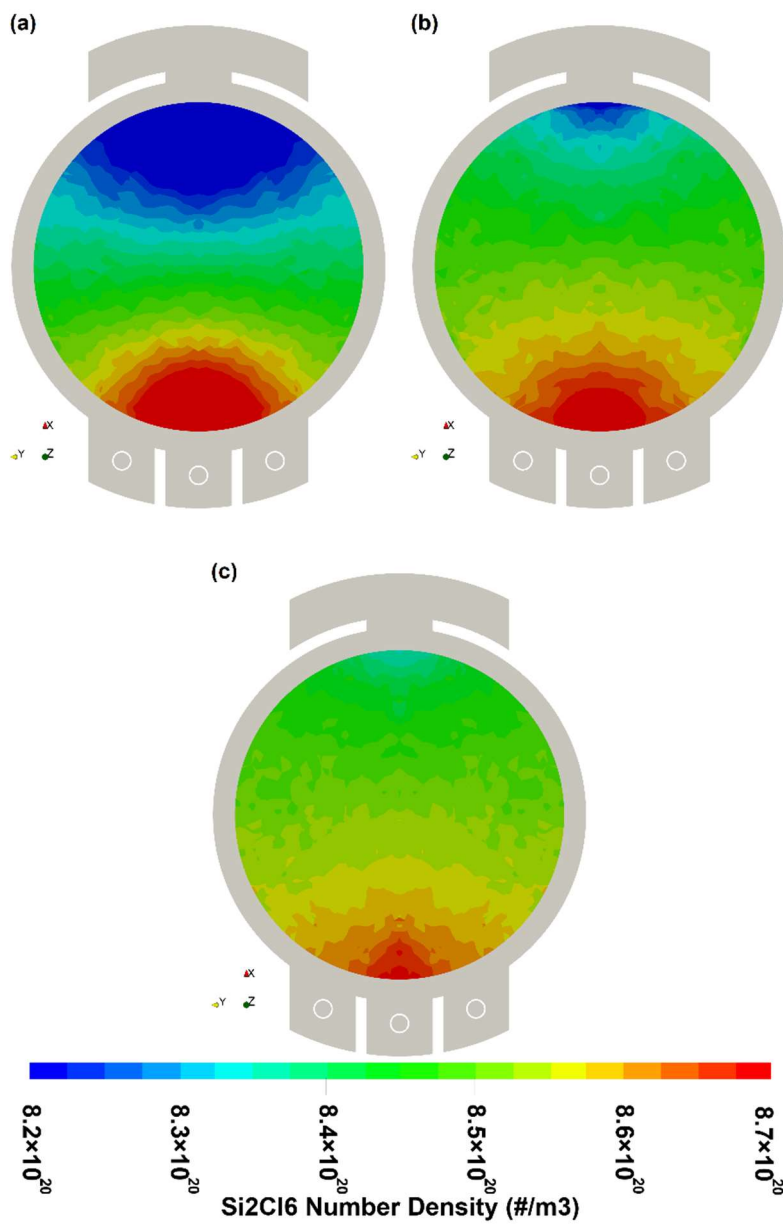


Figure 3.6: Cross sections of (a) #4, (b) #13, and (c) #22 wafers showing number density profiles of HCD for lowest pressure (43Pa). [Note the simulation results are mirrored about the half plane for clarity]

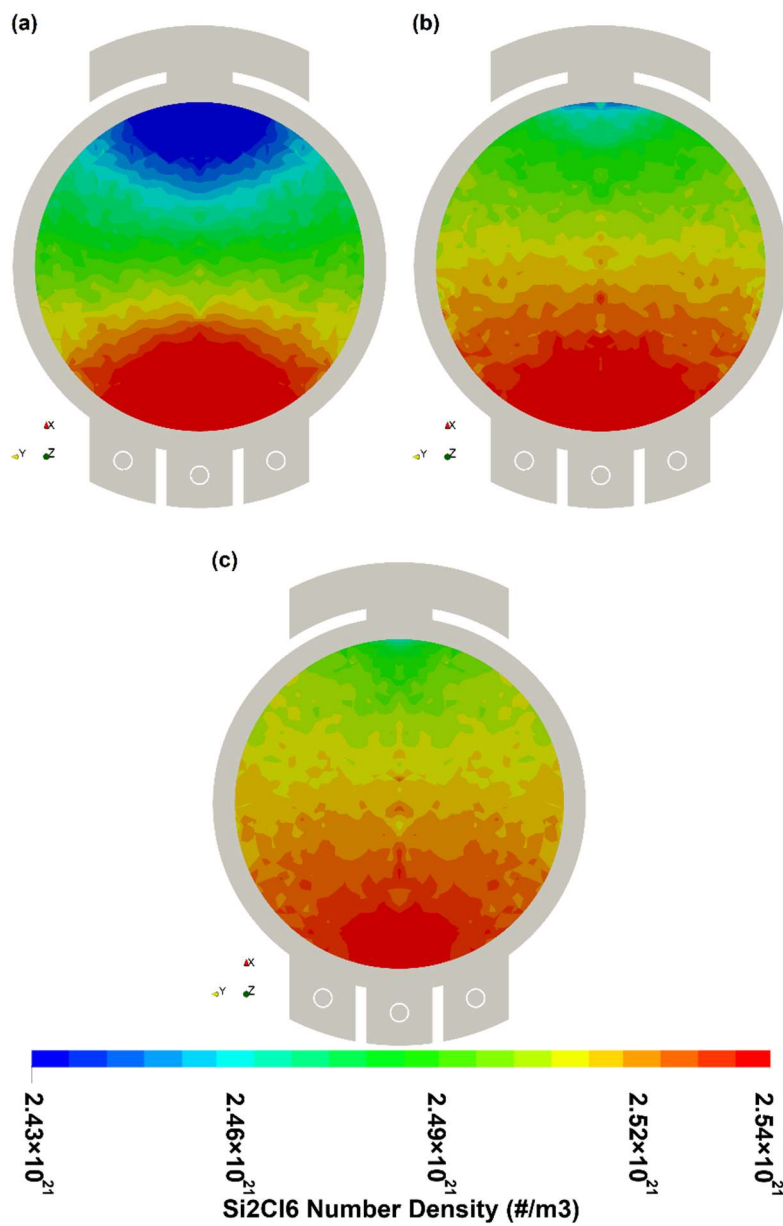


Figure 3.7: Cross sections of (a) #4, (b) #13, and (c) #22 wafers showing number density profiles of HCD for intermediate pressure (86 Pa). [Note the simulation results are mirrored about the half plane for clarity]

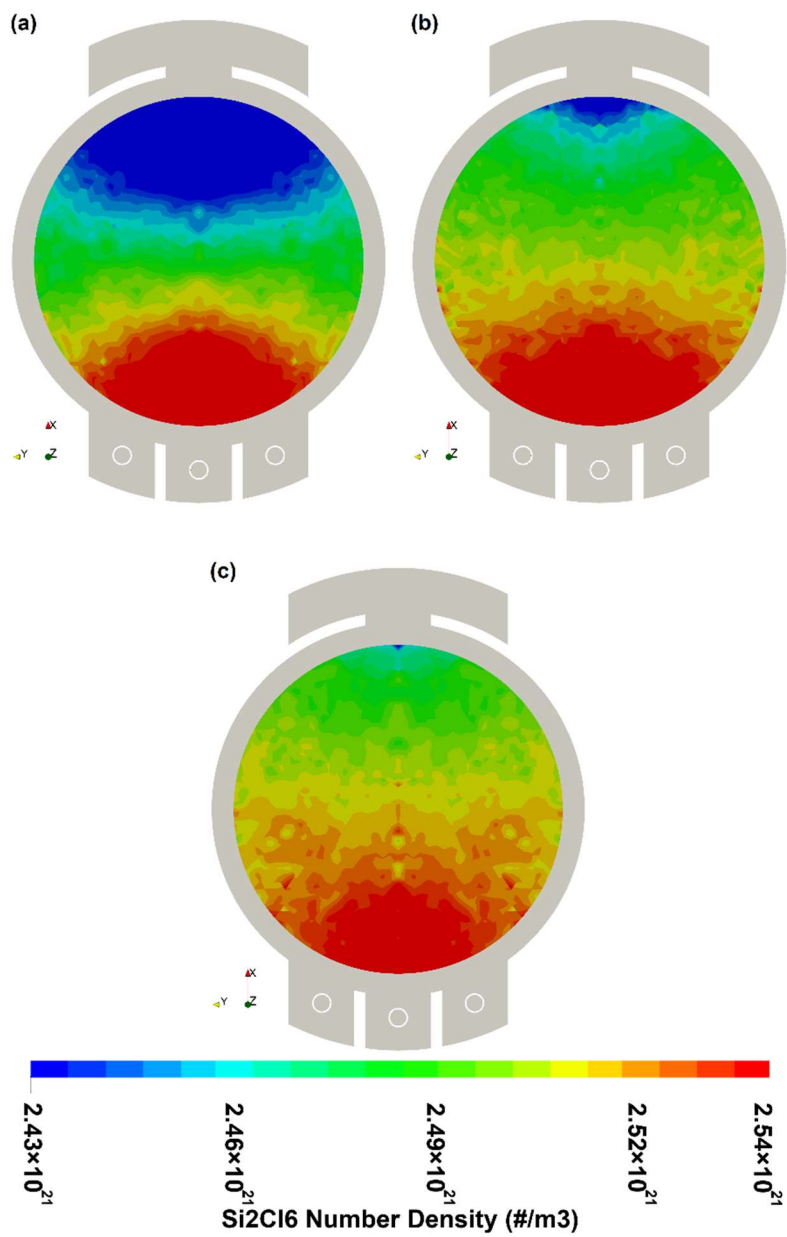


Figure 3.8: Cross sections of (a) #4, (b) #13, and (c) #22 wafers showing number density profiles of HCD for highest pressure (130Pa). [Note the simulation results are mirrored about the half plane for clarity]

The effect of gas mixing between the HCD and side inlet N<sub>2</sub> streams can be discerned in Figures 3.6, 3.7 and 3.8, where the inter-wafer HCD density profiles are shown for 3 wafer locations near the bottom (4<sup>th</sup>), middle (13<sup>th</sup>) and top (22<sup>nd</sup>) of the stack, for all three cases. The locations of the central inlet nozzle, side inlet nozzle, and the annular bypass flow regions are shown for clarity. As seen in the flow streamlines in panel (c) of Figure 3.4, the flow from the central inlet that carries the HCD molecules expands sideways as it enters the reactor volume. This sideways flow of the central gas is however confined by the side inlet with the pure N<sub>2</sub> gas streams that forces the HCD laden flow into the inter-wafer gap region, thereby minimizing the loss of HCD molecules down the annular bypass region. The evidence for this central inlet flow confinement by the side inlet streams is directly visible in the inter-wafer HCD density profiles in Figures 3.6, 3.7 and 3.8. The maximum HCD densities are seen in the nozzle inflow region spanning the regions between left and the right-side inlets in all cases with an abrupt drop in densities beyond this region. Therefore, it is reasonable conclude that an important role of the side inlet streams is to prevent loss of HCD precursors to the bypass flow and maximize active precursor gas exposure to the wafer processing surface. Additionally, Figures 3.6, 3.7 and 3.8 illustrate the bottom-most wafers experience the highest HCD densities

close to the nozzle inflow region and minimum HCD densities at the opposite end close to the outflow region. The HCD density distribution over the wafer surfaces is more uniform for the top-most inter-wafer regions. Upon comparing the low pressure 43 Pa case to the high pressure 130 Pa case, the non-uniformity, as characterized by the difference between the maximum and minimum densities to the average densities in the inter-wafer regions, is lower for the lower pressure cases. This trend is expected since lower pressures promote greater diffusion of species thereby improving uniformity.

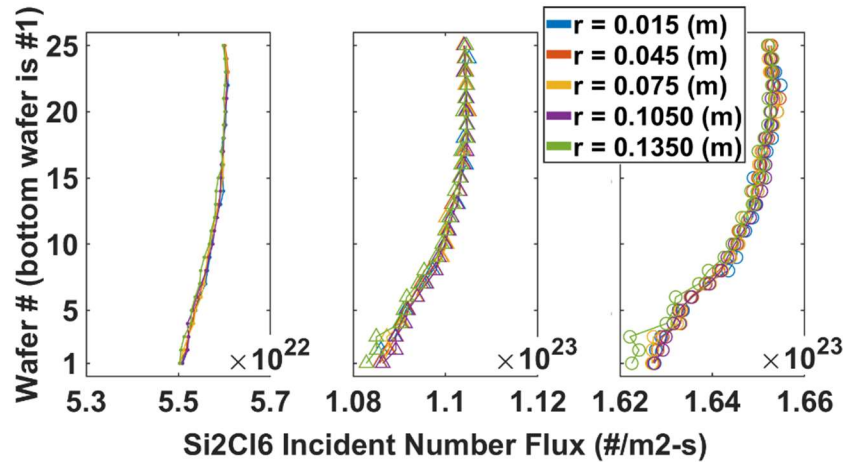


Figure 3.9: Azimuthally averaged incident surface flux of HCD ( $\#/m^2\text{-s}$ ) sampled at various locations on the wafers for all three pressure cases.

The non-uniformities in the HCD densities over the wafer surfaces seen in Figures 3.6, 3.7 and 3.8, emphasize the need for improving the uniformity by mechanical rotation of the wafer stack. In fact, in the absence of rotation, the non-uniformity is not acceptable for production manufacturing. Figure 3.9 shows the azimuthally averaged flux of HCD precursor molecules impacting the wafer surface for three pressure cases and at different radial location on the wafer. The average precursor species flux to the surface increases going from the bottom-most wafer to the top-most wafer in all three pressure cases. The absolute values of the precursor flux are about  $5.6 \times 10^{22}$  #/m<sup>2</sup>-s in the 43 Pa case and increases to about  $1.65 \times 10^{23}$  #/m<sup>2</sup>-s in the 130 Pa case, i.e., an increase that is proportional to the pressure. The single wafer non-uniformity is seen to be the lowest for the lowest pressure case and increases with increasing pressures. The highest single-wafer non-uniformity is observed for the bottom-most wafer in the 130 Pa case and even here the non-uniformity is only about 0.6%. The cross-wafer non-uniformity in the wafer stack is nearly the same in all pressure cases at about 1%.

### 3.3 Precursor-Wafer Interaction Efficiency

Precursor gases such as the one described above can add significantly to the overall operating cost in an ALD process. Besides, precursors molecules can often be toxic and environmentally damaging. Consequently, the efficient utilization of precursor molecules is an important process metric. For the multi-wafer ALD reactor, a parameter called the precursor-wafer interaction efficiency is defined as the fraction of inlet HCD molecules that have interacted one or more of the wafer surfaces at least once during their residence in the reactor volume. Here the precursor-wafer interaction efficiency is given as,

$$\eta_{HCD} = \frac{\dot{N}_{out,wafer}}{\dot{N}_{out,total}} \quad (6)$$

where  $\dot{N}_{out,wafer}$  is the number flow rate of HCD molecules at the outlet that have reflected the wafer surfaces at least once to the total number flow rate of the HCD molecules at the outlet  $\dot{N}_{out,total}$  (which equals the inflow rate of the HCD molecules).

In order to identify the HCD molecules that have visited the wafer surfaces at least once, simulations were run where HCD molecules that impacted any one of the active wafer surfaces are tagged and allowed to

continue on their trajectories through the reactor with no change to their properties. These tagged HCD molecules are then counted at the outlet surface and their ratio with the total HCD molecules (tagged plus untagged) are used to determine the precursor utilization efficiency.

Results indicate an interaction efficiency in excess of 99% for all cases reported in this work. This implies that the ALD reactor designs with the multi-wafer stacks, with independent nozzle feeds for each inter-wafer gap, including the central inlet with the active HCD laden flow along with two side inlets with the inert carrier gas are highly efficient in terms of precursor-wafer interaction.

## Chapter 4

### Summary

A DSMC study of a multi-species flow phenomena in a low-pressure 25-wafer batch ALD reactor is presented in this study. Three reactor pressure cases were simulated: 43 Pa, 86 Pa, and 130 Pa. The reactor walls and wafers are specified as diffusely reflecting isothermal surfaces maintained at 873 K. The feed gas mixture consists of carrier  $N_2$  and precursor HCD. The volume flow ratios of the of the gas mixture are kept constant across all three cases. A computation mesh of 1.2 million tetrahedral cells was used to represent the reactor geometry and about 15 million simulated particles was used in the DSMC simulation. The steady state results were ensured by simulating each case for  $\sim 8.5$  s, twenty times longer than the slowest residence time for this reactor.

Results in the vicinity of wafers indicate high Knudsen numbers ( $\sim 0.2$ ) corresponding to slip regime, thus justifying the use of DSMC to accurately characterize flow in the reactor. For all three cases, the flow inside the nozzles was high subsonic inviscid flow and therefore unchoked. However, it quickly transitions to viscous dominated Stokes flow within the inter-wafer

gap regions. The use of a three-inlet design with precursor HCD laden central inlet and the inert N<sub>2</sub> gas side inlets is clarified by the results. The roles of side inlets are seen to promote confinement of the central inlet flow thereby minimizing bypass of this flow and directing the precursor into the inter-wafer gap. The utilization of the precursor gases is therefore maximized by this design. The observed precursor-wafer interaction efficiency was ~99% for all three operating pressures.

The pressure, temperature, and concentration of the precursor were all predicted to have a maximum variation of 1% WiW, and 2% WTW. The highest non-uniformity both WiW and WTW was observed in the higher pressure 130 Pa case. The lower-most wafer in every case had the highest pressure and the highest exposure to the precursor HCD molecules.

In conclusion, the need for a particle-based simulation approach for low-pressure industrial ALD reactors used in modern semiconductor manufacturing processes is demonstrated. The multi-species DSMC approach with complex geometry representation is necessary and shown to be effective for accurate quantitative modeling, design, and optimization of these reactors.

## 4.1 Future Work

Temperature and pressure spatial uniformity heavily influence the transport kinetics and surface reactions. High temperature and pressure conditions are known to cause decomposition in  $\text{Si}_2\text{HCl}_5$  [11][28][29], a precursor similar to  $\text{Si}_2\text{Cl}_6$ . This prompts the question of premature decomposition of  $\text{Si}_2\text{Cl}_6$  in the feed pipes where pressure and temperature were highly favorable for such reactions. Understanding these effects are crucial in determining the constituents' concentration after the decomposition of the precursor gas to accurately model surface reactions at a much smaller scale, for example, at the trench level. Results inferred from this paper can be used to model trench-scale reactive mechanisms focusing on the effects of pressure and temperature on decomposition of the precursor  $\text{Si}_2\text{Cl}_6$ , formation of Si-complexes on trench surfaces, and growth per cycle estimations.

## References

- [1] B. Prince, Vertical 3D Memory Technologies, John Wiley & Sons, Incorporated, 2014, pp. 23-24.
- [2] E. Granneman, P. Fischer, D. Pierreux, H. Terhorst and P. Zagwijn, "Batch ALD: Characteristics, comparison with single wafer ALD, and examples," *Surface & coatings technology*, vol. 201, no. 22-23, pp. 8899-8907, 2007.
- [3] R. W. Johnson, A. Hultqvist and B. S. F., "A brief review of atomic layer deposition: from fundamentals to applications," *Materials Today*, vol. 17, no. 5, pp. 236-246, 2014.
- [4] M. Leskela and M. Ritala, "Atomic Layer Deposition Chemistry: Recent Developments and Future Challenges," *Angewandte Chemie*, vol. 42, no. 45, pp. 5548-5554, 2003.
- [5] X. Meng, Y.-C. Byun, H. Kim, J. Lee, A. Lucero, L. Cheng and J. Kim, "Atomic Layer Deposition of Silicon Nitride Thin Films: A Review of Recent Progress, Challenges, and Outlooks," *Materials*, vol. 9, no. 12, p. 1007, 2016.
- [6] S. M. George, "Atomic Layer Deposition: An Overview," *Chemical reviews*, vol. 110, no. 1, pp. 111-131, 2010.
- [7] R. J. Kee, W. Yang, L. L. Raja and C. A. Wolden, "The influence of pressure, fluid flow, and chemistry on the combustion-based oxidation

- of silicon," *Proceedings of the Combustion Institute*, vol. 28, no. 1, pp. 1381-1388, 2000.
- [8] R. Rupp, A. Wiedenhofer and D. Stephani, "Epitaxial growth of SiC in a single and a multi wafer vertical CVD system: a comparison," *Materials science & engineering*, vol. 61, pp. 125-129, 1999.
- [9] H. Horita, T. Yotsutani and T. Ozaki, "Substrate processing apparatus, method of manufacturing semiconductor device, and recording medium". United States of America Patent US 2020/0024731 A1, 23 January 2020.
- [10] H. Yoshida, S. Odake, T. Taniyama and T. Nakada, "Substrate Processing Device, Manufacturing Method for Semiconductor Device, and Reaction Tube". United States of America Patent US 2019/0393045 A1, 26 December 2019.
- [11] E. Solmaz, S.-M. Ryu, J. Uh and L. Raja, "Surface kinetics and feature scale particle model of SixNy atomic layer deposition using Si<sub>2</sub>Cl<sub>6</sub> precursor," *J. of Vac. Sci. Technol. A*, vol. 38, p. 052405, 2020.
- [12] T. Iwao, P. L. G. Ventzek, R. Upadhyay, L. L. Raja, H. Ueda and K. Ishibashi, "Measurements and modeling of the impact of radical recombination on silicon nitride growth in microwave plasma assisted atomic layer deposition," *Journal of Vacuum Science & Technology*, vol. 36, no. 1, p. 1, 2018.
- [13] M. G. Crose, "Multiscale Computational Fluid Dynamics Modeling:

Parallelization and Application to Design and Control of Plasma-Enhanced Chemical Vapor Deposition of Thin Film Solar Cells," UCLA Electronic Theses and Dissertations, Los Angeles, 2018.

- [14] D. Pan, L. Ma, Y. Xie, F. Wang, T.-C. Jen and C. Yuan, "Experimental and numerical investigations into the transient multi-wafer batch atomic layer deposition process with vertical and horizontal wafer arrangements," *International journal of heat and mass transfer*, vol. 91, no. 12, pp. 416-427, 2015.
- [15] M. R. Shaeri, T.-C. Jen and C. Y. Yuan, "Reactor scale simulation of an atomic layer deposition process," *Chemical engineering research & design*, vol. 94, no. 2, pp. 584-593, 2015.
- [16] S. W. King, "Plasma enhanced atomic layer deposition of SiN<sub>x</sub>:H and SiO<sub>2</sub>," *Journal of vacuum science & technology*, vol. 29, no. 4, p. 41501, 2011.
- [17] A. Lankhorst, B. Paarhuis, H. Terhorst, P. Simons and C. Kleijn, "Transient ALD simulations for a multi-wafer reactor with trenched wafers," *Surface & coatings technology*, vol. 201, no. 22, pp. 8842-8848, 2007.
- [18] R. A. Adomaitis, "Development of a multiscale model for an atomic layer deposition process," *Journal of crystal growth*, vol. 312, no. 8, pp. 1449-1452, 2010.
- [19] V. H. Dwivedi, "A Multiscale Model for an Atomic Layer Deposition

Process," University of Maryland, Maryland, VA, 2010.

- [20] B. E. Rapp, *Microfluidics : modeling mechanics and mathematics*, Amsterdam, Netherlands: William Andrew, 2017.
- [21] G. A. Bird, *Molecular Gas Dynamics and the Direct Simulation of Gas Flows*, Oxford: Clarendon Press, 1994.
- [22] K. Park, W.-D. Yun, B.-J. Choi, H.-D. Kim, W.-J. Lee, S.-K. Rha and C. O. Park, "Growth studies and characterization of silicon nitride thin films deposited by alternating exposures to Si<sub>2</sub>Cl<sub>6</sub> and NH<sub>3</sub>," *Thin solid films*, vol. 517, no. 14, pp. 3975-3978, 2009.
- [23] R. A. Ovanesyan, E. A. Filatova, S. D. Elliott, D. M. Hausmann, D. C. Smith and S. Agarwal, "Atomic layer deposition of silicon-based dielectrics for semiconductor manufacturing: Current status and future outlook," *Journal of Vacuum Science & Technology A: Vacuum, Surfaces, and Films*, vol. 37, no. 6, p. 60904, 2019.
- [24] VizGrain - A Simulator for Rarefied Gas, Macroscopic Particle and Hybrid Plasma Dynamic Simulations, User Manual v2.4, Austin, TX: Esgee Technologies, 2020.
- [25] D. Levko, R. R. Upadhyay, D. Breden, A. Karpatne and L. L. Raja, "VizGrain: A new computational tool for the modeling of reactive plasma discharges and rarefield flow physics," *Plasma Sources Science Technologies*, p. (in review), 2020.

- [26] "Salome - The Open Source Integration Platform for Numerical Simulation," 2020. [Online]. Available: <https://www.salome-platform.org/>. [Accessed 7 March 2020].
- [27] Z.-X. Sun, Z. Tang, Y.-L. He and W.-Q. Tao, "Proper cell dimension and number of particles per cell for DSMC," *Computers & fluids*, vol. 50, no. 1, pp. 1-9, 2011.
- [28] S. Ravasio, M. Masi and C. Cavallotti, "Analysis of the Gas Phase Reactivity of Chlorosilanes," *The journal of physical chemistry*, vol. 117, no. 25, pp. 5521-5231, 2013.
- [29] K. L. Walker, R. E. Jardine, M. A. Ring and H. E. O'Neal, "Mechanisms and kinetics of the thermal decompositions of trichlorosilane, dichlorosilane, and monochlorosilane," *International journal of chemical kinetics*, vol. 30, no. 1, pp. 69-88, 1998.
- [30] D. W. Breck, "Zeolite Molecular Sieves: Structure, Chemistry, and Use," *Journal of Chromatographic Science*, vol. 13, no. 4, p. 18, 1975.
- [31] F. Sharipov, "Numerical simulation of turbomolecular pump over a wide range of gas rarefaction," *Journal of vacuum science & technology*, vol. 28, no. 6, pp. 1312-1315, 2010-2011.
- [32] VizGlow - Plasma Modeling Software for Multi-Dimensional Simulations of Non-Equilibrium Glow Discharge Systems, User Manual v2.4, Austin, TX: Esgee Technologies, 2020.

## **Vita**

Sudharshanaraj Thiruppathiraj, son of Thiruppathiraj Rengasamy and Uma Rani Thiruppathiraj, was born in Srivilliputhur, India in 1995. He has a younger sister Raji Dharshini Thiruppathiraj.

He started studying mechanical engineering at Tennessee Technological Institute in August 2013. After transferring to the Department of Aerospace Engineering and Engineering Mechanics at The University of Texas at Austin, he eventually obtained his Bachelor of Science in aerospace engineering in May 2018. He returned to The University of Texas at Austin in January 2019 to pursue his Master of Science in aerospace engineering.

Permanent address: [raj\\_utaustin@utexas.edu](mailto:raj_utaustin@utexas.edu)

This thesis was typed by the author.